Nanoscale Horizons

ROYAL SOCIETY OF CHEMISTRY

COMMUNICATION

View Article Online
View Journal | View Issue

Cite this: *Nanoscale Horiz.*, 2025, **10**, 2447

Received 28th April 2025,
Accepted 30th June 2025

DOI: 10.1039/d5nh00274e

rsc.li/nanoscale-horizons

Upscaled wood@MoS_2/Fe_3O_4 bulk catalysts for sustainable catalytic water pollutant removal†

Lingli Zhu, Wei Ren,* Ya Liu, Zhong-Shuai Zhu, Shuang Zhong, Shaobin Wang and Xiaoguang Duan *

Advanced oxidation processes (AOPs) play a pivotal role in purifying contaminated water and securing drinking water safety. Transition metal-based materials are highly effective AOP catalysts, while their applications are limited by their poor stability in the oxidative environment. In this study, we developed a composite catalyst, molybdenum disulfide/ferric oxide (MoS_2/Fe_3O_4), to evaluate its catalytic performance and explore its underlying mechanisms in peroxymonosulfate activation. The powder composite was successfully loaded onto an engineered wood substrate, creating a monolith wood@MoS_2/Fe_3O_4 composite for large-scale practical applications. The engineered bulk catalyst exhibits exceptional versatility and stability in wastewater treatment, maintaining nearly 100% removal efficiency over continuous operation for 144 hours. These findings underscore the significant potential of wood-loaded nanomaterials for cost-effective wastewater treatment.

New concepts

Advanced oxidation processes (AOPs) are among the most promising strategies for eliminating recalcitrant organic pollutants in wastewater. However, their real-world application is hindered by the poor recoverability and stability of conventional powder-form nanocatalysts. In this work, we present a scalable and sustainable strategy to overcome this bottleneck by anchoring a MoS_2/Fe_3O_4 nanocomposite onto delignified natural wood, resulting in a monolithic wood@MoS_2/Fe_3O_4 bulk catalyst. This bio-derived structure leverages the hierarchical porosity of wood to support active catalytic components while enabling high mass transfer efficiency and operational stability. The resulting catalyst achieves nearly 100% removal of antibiotic contaminants over 144 hours of continuous operation, exhibiting outstanding resilience across a wide pH range and in the presence of diverse coexisting species. Mechanistic studies confirm that the composite activates peroxymonosulfate primarily through hydroxyl radical generation, with MoS_2 enhancing Fe redox cycling *via* interfacial electron transfer. By combining nanomaterial functionality with macroscopic engineering, this work provides a robust platform for practical, low-cost, and reusable AOP catalysts and highlights the potential of biomass-derived supports for environmental nanotechnology.

1. Introduction

Sustainable water and sanitation management has been a global priority.[1,2] However, due to inadequate wastewater treatment facilities, particularly in low-income regions, it remains a significant challenge to achieve effective recycling and safe reuse of water resources.[3] Conventional wastewater treatment methods, including biological, physical, and chemical processes, have proven insufficient in removing complex pollutants, especially those originating from industrial and pharmaceutical sources. This limitation underscores the urgent need for advanced treatment technologies that can effectively mitigate environmental and public health risks. In this context, advanced oxidation processes (AOPs) have emerged as a promising solution to the degradation of recalcitrant pollutants, such as antibiotics.[4] In AOPs highly reactive species are generated, including hydroxyl ($^{\bullet}OH$)[5] and sulfate radicals ($SO_4^{\bullet-}$),[6,7] which possess strong oxidative potentials and can non-selectively oxidize a wide range of organic pollutants[8,9] by breaking them down into harmless end-products such as water, carbon dioxide, and inorganic ions.[10]

Conventional homogeneous AOPs face challenges such as low efficiency, high energy consumption and a narrow effective pH range, which can be addressed by using heterogeneous catalysts to minimize metal usage and potential leaching.[11,12] Among the extensively studied materials, Fe- and Mo-based catalysts have attracted considerable attention due to their high availability, eco-friendliness, cost-effectiveness, and efficiency.[13,14] Their efficiency in AOPs is typically influenced by various factors, including the nature and accessibility of active sites, surface area and porosity, as well as electron-transfer capacity of the catalysts.[15] However, most Fe- and Mo-based heterogenous catalysts are used in the powder form, which limits their application in practical wastewater treatment because of the difficulty in recovery and

School of Chemical Engineering, The University of Adelaide, Adelaide, SA 5005, Australia. E-mail: wei.ren@adelaide.edu.au, xiaoguang.duan@adelaide.edu.au

† Electronic supplementary information (ESI) available. See DOI: https://doi.org/10.1039/d5nh00274e

reusability, as well as the potential to introduce secondary contamination, particularly for nanomaterials.[16]

Therefore, developing a high-performance and stable upscaled catalyst is crucial for achieving superior performance, reusability, and industrial-scale applications.[17,18] To the best of our knowledge, upscaled catalysts normally exhibit poor performance due to a lower specific surface area and limited exposure of active components.[19] Wood, as a renewable, low-cost, and structurally robust material, presents unique advantages as an upscaled engineered catalyst support in AOPs for water pollutant remediation. Its naturally occurring three-dimensional porous network not only offers a high surface area for catalyst dispersion but also enhances mass transfer and facilitates pollutant accessibility to catalytic sites.[20] Moreover, the hierarchical architecture of wood, with interconnected micro- and macropores, ensures efficient reactant transport and mitigates diffusion limitations commonly observed in conventional powder-based catalysts.[21] In this study, we introduce a composite catalyst, integrating molybdenum disulfide (MoS_2) nanoflowers with iron oxide (Fe_3O_4) as MoS_2/Fe_3O_4 heterostructures to activate peroxymonosulfate (PMS) for antibiotic degradation. Furthermore, we loaded this active composite onto a treated wood framework to enhance the mass transfer of reactants and scalability of the powder catalysts to be used in a bulk form, making it suitable for continuous wastewater treatment.

2. Materials and methods

2.1. Chemicals and reagents

All analytical-grade chemicals were supplied by Sigma, and the details are presented in the ESI,† Section S1.1.

2.2. Preparation of MoS_2/Fe_3O_4 and wood@MoS_2/Fe_3O_4 composites

2.2.1. Preparation of the MoS_2/Fe_3O_4 composite. The specific preparation method is as follows: 0.9073 g of $Na_2MoO_4 \cdot 2H_2O$, 0.8564 g of CN_2H_4S, 0.8806 g of ascorbic acid and 0.32 g of $FeCl_3 \cdot 6H_2O$ were dissolved in deionized water by ultrasound treatment and then magnetically stirred for 30 min. The mixture was transferred into a 50 mL Teflon-lined hydrothermal kettle and reacted at 200 °C for 24 h. Finally, the solid obtained was washed and centrifuged with deionized water and absolute ethanol several times.

2.2.2. Preparation of the wood@MoS_2/Fe_3O_4 composite. According to the method previously reported by Hu *et al.*,[22,23] the wood@MoS_2/Fe_3O_4 composite was successfully prepared. First, natural wooden blocks were immersed in a boiled solution of mixed 2.5 M NaOH and 0.4 M $NaSO_3$ for 3 h, followed by immersion in deionized water several times to dissolve part of the lignin content using the chemicals and processes in kraft pulping. Next, the wooden blocks were transferred into H_2O_2 solution to remove the remaining lignin. Since lignin is colored while cellulose is colorless, the color in the wooden blocks indicates the amount of lignin present on the wooden block surface; then the wooden blocks were washed with deionized water and freeze dried to obtain the treated wood. The treated wood was then immersed in a MoS_2/Fe_3O_4 solution for loading MoS_2/Fe_3O_4 using ultrasound treatment. After being dried in an oven at 200 °C, these blocks were further calcined in a tube furnace at 500 °C for 2 h (under a nitrogen atmosphere) to obtain the wood@MoS_2/Fe_3O_4 composite.

2.3. Characterization of catalysts

X-ray powder diffraction (XRD) patterns were obtained on a Rigaku MiniFlex 600 X-ray diffractometer. Scanning electron microscopy (SEM) images were collected on a FEI Quanta 450 FEG environmental scanning electron microscope. Transmission electron microscopy (TEM) images were collected on an FEI Tecnai G2 Spirit TEM. High angle annular dark-field scanning TEM (HAADF-STEM) images with EDS elemental mapping was obtained on a FEI Titan Themis 80–200 operating at 200 kV. The porous structures of the obtained catalysts were analyzed using nitrogen adsorption–desorption isotherms *via* the Brunauer–Emmett–Teller (BET, Micromeritics ASAP 2460, USA) method. Raman spectra were measured using a Raman spectroscopy instrument (Horiba Scientific, Germany) equipped with a laser emitting at 532 nm. X-ray photoelectron spectroscopy (XPS) spectra were collected using a Thermo Scientific K-Alpha. Co K-edge X-ray absorption spectroscopy (XAS) analysis was carried out under ambient conditions. Both X-ray absorption near-edge structure (XANES) spectra and extended X-ray absorption fine structure (EXAFS) spectra were acquired at the Australian Synchrotron in Melbourne.

3. Results and discussion

3.1. Characterization of catalysts

Fig. 1 presents SEM images of MoS_2 (Fig. 1a and b) nanoflowers and MoS_2/Fe_3O_4 composites (Fig. 1c) at different magnifications. MoS_2 could retain its characteristic nanoflower structure after the incorporation of Fe_3O_4. The TEM image of MoS_2/Fe_3O_4 (Fig. 1d) further confirms the successful combination of Fe_3O_4 with the ultrathin MoS_2 nanosheets. Additionally, the HRTEM image (Fig. 1e–h) reveals lattice fringes with an interlayer distance of 473 pm, corresponding to the (111) plane of Fe_3O_4 nanoparticles.[24] The lattice spacings of 652 pm and 272 pm

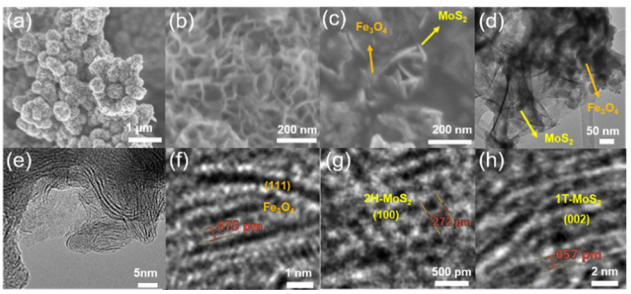

Fig. 1 SEM images of (a) and (b) MoS_2 and (c) MoS_2/Fe_3O_4 nanoparticles and (d) TEM image and (e)–(h) HRTEM images of MoS_2/Fe_3O_4 nanoparticles.

correspond to the (002) and (100) planes of 1T- and 2H-MoS_2 phases, respectively.[25,26] Notably, 1T-MoS_2 exhibits approximately 10^7 times greater electrical conductivity than 2H-MoS_2,[27] which will significantly enhance the electron transfer processes in AOP catalysis.

To further examine the crystalline phases and chemical composition of catalysts, we conducted a series of material, structural and chemical analyses, including X-ray diffraction (XRD), Raman spectroscopy, X-ray photoelectron spectroscopy (XPS), and electron paramagnetic resonance (EPR) spectroscopy. As shown in Fig. 2a, a prominent peak of MoS_2/Fe_3O_4 at 8.0°, corresponding to the (002) plane of 1T-MoS_2, was observed. Additionally, the peaks at 2θ values of 15.3°, 32.9°, and 58.3° correspond to the MoS_2 Bragg planes of (004), (100), and (110), respectively.[4,28] Other peaks located at 20°, 26.2°, 35.6°, 43°, and 56.3° were assigned to the Fe_3O_4 Bragg planes of (111), (220), (311), (400), and (511), respectively. In comparison with standard diffraction data (PDF#89-4319 and #75-1539), the measured lattice spacings of 0.48 nm, 0.27 nm, and 0.65 nm (Fig. 1f–h) correspond to the (111) and (100) planes of Fe_3O_4 and the (002) plane of MoS_2, respectively, based on the Scherrer equation (eqn (1)):

$$d = \lambda/(2\sin\theta) \quad (1)$$

where d represents the lattice spacing, λ was 1.5406 Å, and θ represents the corresponding diffraction angle of the material.

After compositing with Fe_3O_4, a significant displacement in some of the MoS_2 peaks was observed. These findings were consistent with the Raman spectra (shown in Fig. 2b), where peaks at 234.7 (J2) and 331.0 cm^{-1} (J3) were attributed to the 1T phase,[29] while the peaks at 216.71, 277.56, 385.60, and 582.30 cm^{-1} were typical features of Fe_3O_4.[30] These findings state that the combination of MoS_2 and Fe_3O_4 is realized by chemical interactions rather than simple physical mixing, which significantly improves the structural robustness and facilitates interfacial electronic communications to regulate the catalytic activity of surface active sites.

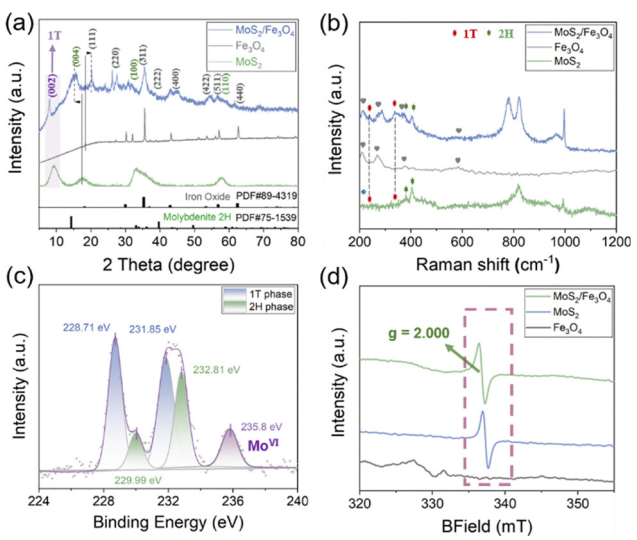

Fig. 2 (a) XRD patterns and (b) Raman spectra of MoS_2, Fe_3O_4 and MoS_2/Fe_3O_4; (c) XPS high-resolution Mo 3d spectra and (d) solid EPR spectra of MoS_2, Fe_3O_4 and MoS_2/Fe_3O_4.

The chemical states of the elements on MoS_2/Fe_3O_4 were further analyzed using XPS, as depicted in Fig. 2c and Fig. S1 (ESI†). Characteristic peaks of Mo, S, and Fe were observed in the XPS full-survey spectra, which reconfirm the successful formation of the MoS_2/Fe_3O_4 composite.[31] Specifically, the binding energies at 228.7 and 231.9 eV correspond to the $3d_{5/2}$ and $3d_{3/2}$ components of 1T-MoS_2, while the peaks at 230 and 232.8 eV were attributed to 2H-MoS_2.[29,32] The proportion of the 1T phase in the MoS_2/Fe_3O_4 composite is determined to be about 60% based on the integrated areas of the corresponding peaks. EPR spectroscopy was used to investigate the effect of Fe_3O_4 on the composite, revealing a slight enhancement of sulfur defect signals around g = 2.000, which is consistent with previous studies.[33,34] The populated defects induced by Fe_3O_4 compositing could act as active sites for binding with the oxygen atoms in peroxide molecules for activation and generation of reactive oxygen species (ROS).

To evaluate the changes in the surface area resulting from the incorporation of Fe_3O_4, we measured nitrogen adsorption/desorption isotherms for both MoS_2 and MoS_2/Fe_3O_4 to determine the BET-specific surface area and pore size distribution (Fig. S2, ESI†). The isotherms exhibited a type-IV adsorption branch with a combination of H1 and H3 hysteresis loops, characteristic of a mesoporous system. The specific surface areas were 10.1 $m^2\ g^{-1}$ for MoS_2 and 10.3 $m^2\ g^{-1}$ for MoS_2/Fe_3O_4. The results suggest that the presence of Fe_3O_4 did not block the porous structures of MoS_2 during the synthesis.

3.2. AOP performance of MoS_2/Fe_3O_4 in PMS activation

3.2.1. Efficiency of the MoS_2/Fe_3O_4 degradation system. To evaluate the performance of the MoS_2/Fe_3O_4 nanocomposite in peroxymonosulfate (PMS) activation and generating ROS, we selected sulfamethoxazole (SMX) as a model contaminant representing persistent antibiotics. As illustrated in Fig. 3 and Fig. S3 (ESI†), the addition of MoS_2/Fe_3O_4 significantly enhances the efficiency in PMS activation, achieving a degradation efficiency of 91.9% within 15 min under optimal conditions. In comparison, MoS_2 nanoparticles alone exhibited a much lower degradation efficiency of 40.2%. Additionally, Fe_2O_3, FeO, and Fe_3O_4 exhibited lower degradation efficiencies (17%, 41.6%, and 40.1%, respectively), further confirming the synergistic effects between MoS_2 and Fe_3O_4 in promoting PMS activation. Notably, the degradation efficiencies of Fe_2O_3 and MoS_2 intersect at 3 minutes, after which MoS_2 exhibits superior performance. This behavior can be attributed to the distinct catalytic mechanisms of the two materials. For MoS_2, PMS must first adsorb onto the exposed active sites on its surface to generate reactive species at the initial stage of the reaction,[35] while additional active sites are progressively formed as the reaction proceeds,[36] leading to a gradual enhancement in catalytic activity. In contrast, the initial high degradation efficiency of Fe_2O_3 is primarily due to surface Fe(II) species that rapidly activate PMS *via* a Fenton-like mechanism. However, as

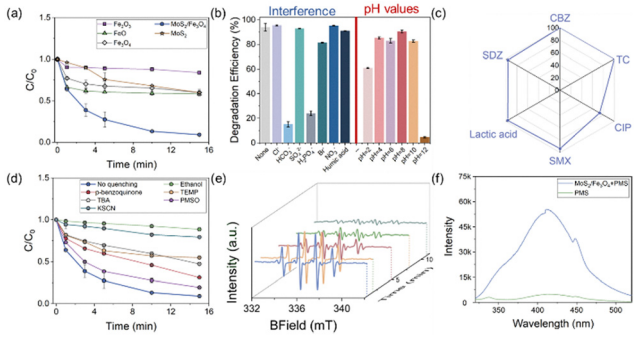

Fig. 3 (a) SMX degradation performances with different catalysts, including Fe_2O_3, FeO, Fe_3O_4, MoS_2 and MoS_2/Fe_3O_4 (reaction conditions: 1.2 mM PMS, 0.08 mM SMX, and 20 mg MoS_2/Fe_3O_4); (b) impacts of organic matter, inorganic ions and different pH values on the removal of SMX in the MoS_2/Fe_3O_4 degradation system; (c) degradation efficiency of different aromatic organic pollutants in 15 min; (d) sacrificial experiments by adding different sacrificial agents into the MoS_2/Fe_3O_4–PMS degradation system; (e) EPR spectra for •OH detection in the presence of 5,5-dimethyl-1-pyrrolidine-*N*-oxide (DMPO) over time at room temperature; (f) the PL intensity of hydroxybenzoic acid in different reaction systems in the presence of benzoic acid as the chemical probe for •OH.

the reaction continues, the limited Fe(II) is quickly depleted, and the inefficient regeneration of Fe(II) from Fe(III) restricts the sustained catalytic activity. These contrasting behaviors result in MoS_2 exhibiting lower activity than Fe_2O_3 in the early stage, but eventually surpassing it, leading to the observed crossover point.

3.2.2. Versatility of the MoS_2/Fe_3O_4 degradation system. Typically, the pH value of wastewater introduces significant limitations for AOPs in pollutant treatment. In Fig. 3b and Fig. S4 (ESI†), we examined the effect of varying initial pH values on the degradation performance. The results indicated that MoS_2/Fe_3O_4 exhibited excellent removal efficiency across a pH range of 4–10, with removal efficiencies between 84.8% and 91.3% closely matching the rate under the initial conditions without pH adjustment (91.9%). However, at extreme pH values (pH 2 or 12), performance declined significantly, with removal rates dropping to 61.4% (pH 2) and 5.1% (pH 12), respectively. This reduction in efficiency may be attributed to a strong pH, which may alter the surface charges of the composite catalyst, affecting its interactions with PMS. Nevertheless, in industrial applications, strong acid/base wastewater typically requires pH adjustment before AOP treatment. The wide pH applicability makes MoS_2/Fe_3O_4 well-suited for practical remediation scenarios.

The presence of different interferents like water matrix constituents (such as HCO_3^-, Cl^-, Br^-, $H_2PO_4^-$, and NO_3^-) and natural organic matter (NOM, such as humic acid) can often impact treatment efficiency *via* scavenging the reactive oxygen species in AOPs.[37–39] Fortunately, most of these constituents had a minimal impact on the MoS_2/Fe_3O_4 degradation system, maintaining removal efficiencies between 81.3% and 95.4% (Fig. 3b and Fig. S5, ESI†). Notably, SMX degradation was prohibited in the presence of HCO_3^- and $H_2PO_4^-$ to 13.8% and 25.3%, respectively. The reduced removal efficiency can be attributed to the alkalinity of HCO_3^- or the coordination of $H_2PO_4^-$ with metal species on the MoS_2/Fe_3O_4 surface, particularly the active Fe site, leading to the surface inactivation of the catalyst.

To assess the versatility of the MoS_2/Fe_3O_4 degradation system, more pollutants, including carbamazepine (CBZ), tetracycline (TC), ciprofloxacin (CIP), and lactic acid, were evaluated. Fig. 3c shows that the system could effectively oxidize these pollutants, with removal efficiencies exceeding 97% for CBZ, TC, and lactic acid. These findings highlight the broad applicability and universal potential of the MoS_2/Fe_3O_4 system in the treatment of diverse organic pollutants in water.

3.2.3. Cycling stability of the MoS_2/Fe_3O_4 degradation system. The stability of the MoS_2/Fe_3O_4 degradation system was evaluated through recycling experiments, as shown in Fig. S6 (ESI†). After each degradation cycle, the catalyst (MoS_2/Fe_3O_4) was recovered and thoroughly washed with deionized (DI) water to remove any residual pollutants from the catalyst surface and reused for subsequent cycles. The removal efficiencies of the first, second, and third cycles were 96.2%, 81.0%, and 76.1%, respectively. These results indicated that the MoS_2/Fe_3O_4 degradation system exhibited satisfactory cycling stability and was resistant to surface deactivation over multiple uses. This robustness makes it a promising candidate in real-world wastewater treatment.

3.2.4. Mechanism in the MoS_2/Fe_3O_4 degradation system. The sacrificial experiments targeting various ROS, such as •OH, $SO_4^{\bullet-}$, $^1O_2$, $O_2^{\bullet-}$, and Fe(IV), were performed by introducing the respective scavengers (Fig. 3d). The results demonstrated that the most significant quenching effects were observed with ethanol and KSCN, reducing the degradation efficiencies to 11.4% and 20.8%, respectively. This indicates that •OH is the primary ROS. The formation of •OH during the reaction was further confirmed by electron paramagnetic resonance (EPR, Fig. 3e) and photoluminescence (PL) (Fig. 3f) spectra. The intensity of •OH characteristic peaks significantly increased after adding the MoS_2/Fe_3O_4 catalyst. The sacrificial experiment also showed a marked reduction in performance when iron sites were complexed with KSCN. However, no Fe(IV) was generated as PMSO showed little quenching effect. This suggests that the presence of Fe_3O_4 enhanced SMX degradation by promoting •OH production, rather than generating high-valent Fe(IV) species. The addition of other scavengers had a minimal impact on SMX degradation, suggesting that $O_2^{\bullet-}$ and $^1O_2$ were not generated or served as the primary ROS during the process, as corroborated by the EPR tests shown in Fig. S7a and b (ESI†).

To further investigate if a nonradical reaction pathway exists in the MoS_2/Fe_3O_4 degradation system, we conducted open-circuit potential (OCP) measurements to assess the charge-transfer process during PMS activation and organic oxidation on the catalyst electrode, without the application of an external potential. Normally, the nonradical oxidation regime is triggered *via* the formation of a nonradical complex (PMS*) with an elevated potential. If the equilibrium potential exceeds the oxidation potential of organic compounds, the complex will gradually oxidize the latter *via* an electron transfer process.[40] As

shown in Fig. S8 (ESI†), the potential of the MoS_2/Fe_3O_4 system remains largely unchanged after the addition of PMS and SMX, compared to that of the bare electrode (no catalyst) system. The results indicate that the primary oxidation mechanism in the MoS_2/Fe_3O_4 system relies on ROS generation, particularly $^{\bullet}OH$.

X-ray photoelectron spectroscopy (XPS) was used to compare the chemical state of Mo in the MoS_2/Fe_3O_4 composite before (Fig. 2c) and after degradation tests (Fig. 4a). A slight shift in the peak position and intensity was observed, with the peak at 233 eV showing a slight reduction, implying that some Mo^{4+} ions were oxidized to Mo^{6+} during the PMS activation. Additionally, X-ray absorption spectroscopy (XAS) was also used to examine the changes in the Fe L-edge of MoS_2/Fe_3O_4 before and after the degradation (Fig. 4b). The two characteristic peaks of Fe_3O_4, located at 707.7 and 709.1 eV, correspond to Fe^{2+} and Fe^{3+}, respectively. After the reaction, a slight increase in Fe^{2+} and a decrease in Fe^{3+} were observed, indicating the participation of Fe_3O_4 in the redox process. The presence of reductive MoS_2 facilitates the redox cycle of iron species *via* electron transfer to Fe_3O_4 to secure a high population of Fe^{2+} species, realizing sustained PMS activation and ROS generation to remove pollutants in multiple runs (Fig. S6, ESI†).

By integrating the ROS test results in Fig. 3 and the state changes of MoS_2 observed in Fig. 4a, the PMS activation mechanism over MoS_2/Fe_3O_4 is illustrated in Fig. 4c. When MoS_2/Fe_3O_4 interacts with PMS, Fe^{2+} on the surface will activate PMS to produce $^{\bullet}OH$, which reacts with and further breaks down pollutants. Simultaneously, the MoS_2 component in the MoS_2/Fe_3O_4 composite facilitates a redox reaction with Fe^{3+} to regenerate Fe^{2+} in Fe_3O_4 *via* interfacial electron transfer, which is essential for sustaining the surface Fe redox cycle for PMS activation, ensuring both durability and efficiency in sustaining pollutant oxidation. Therefore, the MoS_2/Fe_3O_4–PMS system has been validated as being highly effective for organic wastewater treatment owing to its outstanding performance.

3.3. Large-scale study of bulk wood@MoS_2/Fe_3O_4

Considering the common limitations of powder catalysts in real-world wastewater treatment, MoS_2/Fe_3O_4 catalysts were loaded onto a three-dimensional (3D) structured wood substrate to create an upscaled engineered bulky catalyst. First, Australian oak was subjected to delignification by soaking it in a mixture of NaOH and Na_2SO_3, which transformed its appearance from brown to white. The wood was then freeze-dried, providing a massive and porous framework for loading the powder catalyst *via* sonication. After calcination at 500 °C, the final product was obtained, with its appearance changing from white to black (Fig. 5a). SEM images further confirmed the structural transformation throughout the preparation process. Before loading MoS_2/Fe_3O_4, the wood channels were arranged in a neat and compact manner, with pipe diameters measuring approximately 10 μm (as shown in Fig. S11, ESI†). After loading MoS_2/Fe_3O_4, a large number of nanoparticles were observed to

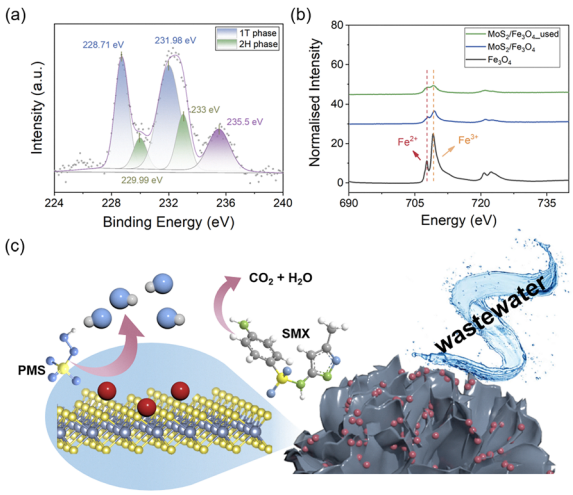

Fig. 4 (a) High-resolution XPS spectra of Mo 3d in MoS_2/Fe_3O_4 after the degradation, (b) Fe L-edge XAS spectra of MoS_2/Fe_3O_4, and (c) the schematic of mechanism of the MoS_2/Fe_3O_4 degradation system.

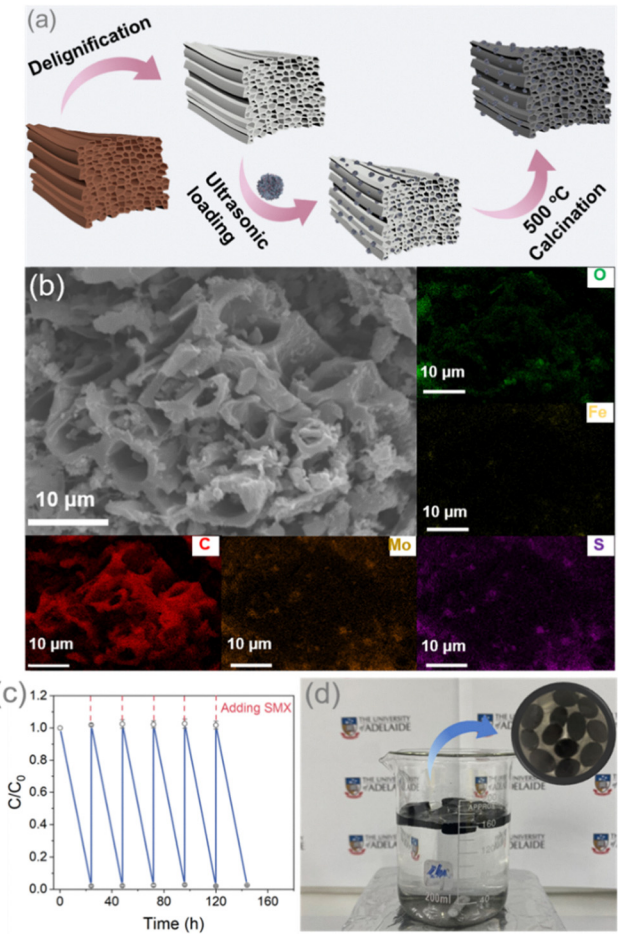

Fig. 5 (a) Illustration of the synthesis of wood@MoS_2/Fe_3O_4; (b) SEM images of wood and wood@MoS_2/Fe_3O_4 and the corresponding EDS elemental mappings; (c) continuous degradation of SMX for 144 h when expanding the degradation system to 150 mL; (d) the facile degradation system using floating wood@MoS_2/Fe_3O_4 as the bulky catalyst.

be dispersed within the wood pores (Fig. 5b and Fig. S9, ESI†), confirming the successful construction of the wood@MoS_2/Fe_3O_4 composite.

In addition, energy-dispersive X-ray spectroscopy (EDS) mapping was conducted to reveal the elemental distribution (Fig. 5b and Fig. S10, S11, ESI†). The analysis clearly displays the presence of C, Mo, S, Fe, and O in the wood@MoS_2/Fe_3O_4 composite. By tracing the distribution, it was found that C and O originated from the wood substrate, while Mo, S, O, and Fe were uniformly distributed in the MoS_2/Fe_3O_4 composite. In comparison, the surface of the wood without catalyst loading appeared much cleaner than that of the wood@MoS_2/Fe_3O_4 composite, and EDS analysis confirmed the uniform distribution of C (Fig. S11, ESI†). These findings fully confirm the successful integration of MoS_2/Fe_3O_4 onto the wood substrate as an upscaled engineered catalyst (wood@MoS_2/Fe_3O_4) for practical use.

Thermogravimetric analysis (TGA) of catalyst blocks (with and without MoS_2/Fe_3O_4) was conducted (Fig. S12, ESI†). The first degradation stage was observed between 100 and 200 °C, which was attributed to moisture release. In this stage, the weight loss of the wood samples before and after catalyst loading decreased by 4.0% (wood) and 3.8% (wood@MoS_2/Fe_3O_4), respectively. The second stage is assigned to the decomposition of lignin occurring in the temperature interval of 400–620 °C.[41] Due to the completion of the delignification process during the preparation, little weight loss was observed here. In the third stage, owing to the high temperature, further carbonization occurred, causing a partial weight loss (about 17.5% and 9.2% for wood and wood@MoS_2/Fe_3O_4, respectively). This is because the loaded MoS_2 nanosheets formed an effective barrier, preventing the wood from combustion.[42] Furthermore, the weight of wood@MoS_2/Fe_3O_4 remained nearly constant above 700 °C, suggesting the chemical and structural robustness of the wood@MoS_2/Fe_3O_4 composites.

In Fig. 5c, the wood@MoS_2/Fe_3O_4 catalyst was evaluated in a continuous degradation experiment to treat SMX in a 150 mL system by refilling SMX regularly over a period of 144 hours. High concentrations of SMX were added every 24 h to maintain the SMX concentration at 20 mg L^{-1}, specifically at time intervals of 0, 24, 48, 72, 96, and 128 h. The results demonstrated that wood@MoS_2/Fe_3O_4 achieved a nearly 100% removal efficiency in each cycle, while PMS only reached about 60% for SMX degradation (Fig. S13, without wood@MoS_2/Fe_3O_4, ESI†), indicating its remarkable effectiveness in SMX degradation. Furthermore, the wood@MoS_2/Fe_3O_4–PMS system can continuously degrade pollutants for 144 h. Fig. 5d shows the wood@MoS_2/Fe_3O_4 catalyst and the corresponding apparatus used in the reaction system, where the catalyst floats on the surface of the wastewater. This floating property makes the catalyst easy to be recovered and reused, significantly enhancing its practicality in real-world applications.

In addition, we further conduct the normalized calculations for wood@MoS_2@Fe_3O_4 in SMX degradation based on the calculation equation (eqn (2)). The result exhibits that the degradation rate constant (K_{value}) was 1.468 min^{-1} M^{-1}, outperforming that of other reported upscaled engineered catalysts shown in Table S1 (ESI†). Notably, in all fairness, all these mentioned catalysts are upscaled engineered catalysts, not simple powder catalysts (the k_{obs} of wood@MoS_2/Fe_3O_4 is shown in Fig. S14, ESI†).

$$K_{value} = k_{obs} \times C_{pollutants}/(C_{catalyst} \times C_{PMS}) \quad (2)$$

where K_{value} represents the total degradation rate constant (min^{-1} M^{-1}); k_{obs} represents the degradation rate constant (min^{-1}), $C_{pollutants}$ represents the concentration of pollutants (mg L^{-1}), $C_{catalyst}$ represents the concentration of metal in the catalyst (g L^{-1}), and C_{PMS} represents the concentration of oxidant (mM).

4. Conclusions

In this work, a MoS_2/Fe_3O_4 composite was successfully synthesized *via* a simple hydrothermal method, which demonstrated excellent catalytic activity in PMS activation for removing a wide spectrum of antibiotics from water. The MoS_2/Fe_3O_4–PMS system exhibited strong resistance to most coexisting inorganic ions and maintained efficiency in a wide pH operation window. Furthermore, the integration of the nanocatalyst onto a porous wood substrate to form a wood@MoS_2/Fe_3O_4 composite enabled the construction of a monolith catalyst, which achieved continuous degradation of organic pollutants and was feasible for easy application and separation. These exceptional properties of Wood@MoS_2/Fe_3O_4 further highlight its potential for large-scale wastewater treatment.

Author contributions

Lingli Zhu: investigation, data curation, and writing – original draft. Wei Ren: methodology, supervision, formal analysis, and writing – review and editing. Ya Liu: investigation. Zhong-shuai Zhu: investigation. Shuang Zhong: methodology. Shaobin Wang: writing – review and editing, resources, and supervision. Xiaoguang Duan: resources, funding acquisition, methodology, writing – review and editing, and supervision.

Conflicts of interest

There are no conflicts to declare.

Data availability

All data generated or analysed during this study are included in this published article.

Acknowledgements

This work was supported by the Australian Research Council (DP230102406, FT230100526 and LE230100168).

Notes and references

1 R. Khosla, N. D. Miranda, P. A. Trotter, A. Mazzone, R. Renaldi, C. McElroy, F. Cohen, A. Jani, R. Perera-Salazar and M. McCulloch, *Nat. Sustainability*, 2021, **4**, 201–208.
2 T. E. T. Dantas, E. D. De-Souza, I. R. Destro, G. Hammes, C. M. T. Rodriguez and S. R. Soares, *Sustainable Prod. Consumption*, 2021, **26**, 213–227.
3 H. M. Delanka-Pedige, S. P. Munasinghe-Arachchige, I. S. Abeysiriwardana-Arachchige, Y. Zhang and N. Nirmalakh andan, *Int. J. Sustainable Dev. World Ecol.*, 2020, **27**, 678–686.
4 L. Zhu, J. Ji, J. Liu, S. Mine, M. Matsuoka, J. Zhang and M. Xing, *Angew. Chem.*, 2020, **132**, 14072–14080.
5 Q. Xu, J. Wu, Y. Qian, X. Chen, Y. Han, X. Zeng, B. Qiu and Q. Zhu, *ACS Appl. Mater. Interfaces*, 2024, **16**, 784–794.
6 Y. Lei, Y. Yu, X. Lei, X. Liang, S. Cheng, G. Ouyang and X. Yang, *Environ. Sci. Technol.*, 2023, **57**, 5433–5444.
7 W. Liu, Y. Lu, Y. Dong, Q. Jin and H. Lin, *Chem. Eng. J.*, 2023, **466**, 143161.
8 R. Fu, P.-S. Zhang, Y.-X. Jiang, L. Sun and X.-H. Sun, *Chemosphere*, 2023, **311**, 136993.
9 X. Liu, X. Yan, W. Liu, Q. Yan and M. Xing, *Sci. Bull.*, 2023, **68**, 603–612.
10 P. Kumari and A. Kumar, *Results Surf. Interfaces*, 2023, **11**, 100122.
11 X. Zheng, X. Niu, D. Zhang, M. Lv, X. Ye, J. Ma, Z. Lin and M. Fu, *Chem. Eng. J.*, 2022, **429**, 132323.
12 B. Liu, B. Huang, Z. Wang, L. Tang, C. Ji, C. Zhao, L. Feng and Y. Feng, *J. Environ. Chem. Eng.*, 2023, **11**, 109586.
13 X. Chen, Y. Chen, S. Li, C. Xue, D. Liu and W. Huang, *Chem. Eng. J.*, 2023, **476**, 146693.
14 J. Liu, C. Peng and X. Shi, *Environ. Pollut.*, 2022, **293**, 118565.
15 J. Wang and J. Tang, *Chemosphere*, 2021, **276**, 130177.
16 L. Jiang, Z. Wei, Y. Ding, Y. Ma, X. Fu, J. Sun, M. Ma, W. Zhu and J. Wang, *Appl. Catal., B*, 2022, **307**, 121184.
17 L. Long, K. Xu, K. B. Tan, D. Cai, Y. Yang, S.-F. Zhou and G. Zhan, *Chem. Eng. Sci.*, 2023, **266**, 118278.
18 P. Brussino, M. S. Gross, M. Ulla and E. D. Banus, *J. Environ. Chem. Eng.*, 2023, **11**, 110858.
19 Q. Peng, W. Zhong, K. Liu and X. Tang, *J. Water Process Eng.*, 2024, **64**, 105700.
20 M. Tian, J. Chen, J. Tian, Z. Liang and Y. Xie, *Mater. Horiz.*, 2025, DOI: **10.1039/D5MH00394F**.
21 T. Yang, H. Zhang, C. Huang, C. Cai, C. Gerhard and K. Zhang, *Small Methods*, 2023, **7**, 2300913.
22 J. Song, C. Chen, S. Zhu, M. Zhu, J. Dai, U. Ray, Y. Li, Y. Kuang, Y. Li and N. Quispe, *Nature*, 2018, **554**, 224–228.
23 M. Zhu, J. Song, T. Li, A. Gong, Y. Wang, J. Dai, Y. Yao, W. Luo, D. Henderson and L. Hu, *Adv. Mater.*, 2016, **28**, 5181–5187.
24 Y. Zhang, P. Chen, F. Wen, B. Yuan and H. Wang, *J. Electroanal. Chem.*, 2016, **761**, 14–20.
25 Y. Peng, M. Geng, J. Yu, Y. Zhang, F. Tian, Y. N. Guo, D. Zhang, X. Yang, Z. Li and Z. Li, *Appl. Catal., B*, 2021, **298**, 120570.
26 X. Wang, Z. Zhang, Y. Chen, Y. Qu, Y. Lai and J. Li, *J. Alloys Compd.*, 2014, **600**, 84–90.
27 S. Wang, D. Zhang, B. Li, C. Zhang, Z. Du, H. Yin, X. Bi and S. Yang, *Adv. Energy Mater.*, 2018, **8**, 1801345.
28 X. Wang, W. Ding, H. Li, H. Li, S. Zhu, X. Zhu, J. Dai, Z. Sheng, H. Wang and X. Zhu, *J. Mater. Chem. A*, 2019, **7**, 19152–19160.
29 H. J. Liu, S. Zhang, Y. M. Chai and B. Dong, *Angew. Chem.*, 2023, **135**, e202313845.
30 J. Geng, Y. Men, C. Liu, X. Ge and C. Yuan, *RSC Adv.*, 2021, **11**, 16592–16599.
31 H. Reddy Inta, T. Biswas, S. Ghosh, R. Kumar, S. Kanti Jana and V. Mahalingam, *ChemNanoMat*, 2020, **6**, 685–695.
32 Q. Liu, Q. Fang, W. Chu, Y. Wan, X. Li, W. Xu, M. Habib, S. Tao, Y. Zhou and D. Liu, *Chem. Mater.*, 2017, **29**, 4738–4744.
33 W. Liu, Y. Dong, J. Liu, L. Zhang, Y. Lu and H. Lin, *Chem. Eng. J.*, 2023, **451**, 138666.
34 H. Geng, Y. Guo, X. Zhang, X. Wang, P. Zhao, G. Wang, J. Liao and L. Dong, available at SSRN 4194501, 2022.
35 J.-C. E. Yang, M.-P. Zhu, X. Duan, S. Wang, B. Yuan and M.-L. Fu, *Appl. Catal., B*, 2021, **297**, 120460.
36 T. Jiang, C. Cai, H. Peng, J. Li, X. Fu, C. Nie and Z. Ao, available at SSRN 5145342.
37 M. Li, Y.-W. Li, P.-F. Yu, H.-M. Zhao, L. Xiang, N.-X. Feng, Q.-K. Li, K.-Y. He, X. Luo and Q.-Y. Cai, *Chem. Eng. J.*, 2022, **427**, 130930.
38 Y. Huang, F. Yang, L. Ai, M. Feng, C. Wang, Z. Wang and J. Liu, *Chemosphere*, 2017, **179**, 331–336.
39 X. Yang, P. Wu, W. Chu and G. Wei, *J. Water Process Eng.*, 2021, **43**, 102231.
40 W. Ren, C. Cheng, P. Shao, X. Luo, H. Zhang, S. Wang and X. Duan, *Environ. Sci. Technol.*, 2021, **56**, 78–97.
41 R. Barzegar, A. Yozgatligil, H. Olgun and A. T. Atimtay, *J. Energy Inst.*, 2020, **93**, 889–898.
42 X. He, L. Zhang, X. Hu and Q. Zhou, *Environ. Sci.: Nano*, 2021, **8**, 2069–2080.